CHEMISTRY
A EUROPEAN JOURNAL

FULL PAPER

DOI: 10.1002/chem.201200434

Electrospun V_2O_5 Nanostructures with Controllable Morphology as High-Performance Cathode Materials for Lithium-Ion Batteries

Heng-guo Wang,[a] De-long Ma,[a, b] Yun Huang,[a, b] and Xin-bo Zhang*[a]

Abstract: Porous V_2O_5 nanotubes, hierarchical V_2O_5 nanofibers, and single-crystalline V_2O_5 nanobelts were controllably synthesized by using a simple electrospinning technique and subsequent annealing. The mechanism for the formation of these controllable structures was investigated. When tested as the cathode materials in lithium-ion batteries (LIBs), the as-formed V_2O_5 nanostructures exhibited a highly reversible capacity, excellent cycling performance, and good rate capacity. In particular, the porous V_2O_5 nanotubes provided short distances for Li^+-ion diffusion and large electrode–electrolyte contact areas for high Li^+-ion flux across the interface; Moreover, these nanotubes delivered a high power density of 40.2 kW kg^{-1} whilst the energy density remained as high as 201 W h kg^{-1}, which, as one of the highest values measured on V_2O_5-based cathode materials, could bridge the performance gap between batteries and supercapacitors. Moreover, to the best of our knowledge, this is the first preparation of single-crystalline V_2O_5 nanobelts by using electrospinning techniques. Interestingly, the beneficial crystal orientation provided improved cycling stability for lithium intercalation. These results demonstrate that further improvement or optimization of electrochemical performance in transition-metal-oxide-based electrode materials could be realized by the design of 1D nanostructures with unique morphologies.

Keywords: cathodes · electrospinning · lithium-ion batteries · nanostructures · nanotubes

Introduction

The rapid development of alternative energy sources and electric transportation has led to significant research efforts being focused towards high-energy- and high-power-density lithium-ion batteries (LIBs).[1] However, even after decades of intensive research, the low capacity of the currently used electrode materials, especially on the cathode side, still seriously hamper its development.[2] There is a general consensus that further enhancements in capacity will require a transition from the currently used Li-insertion/deinsertion compounds, which are limited to 1 e^-/formula-unit, to new compounds that are based on multi-electron-reaction materials.[3–7]

Vanadium pentoxide (V_2O_5), as one of the most-attractive multifunctional materials, has potential applications in the fields of actuators,[8] catalysis,[9] and sensors,[10] as well as in multi-electron battery materials. Since the reversible multi-electron electrochemical lithium-ion intercalation in V_2O_5 was first reported in 1976 by Whittingham,[11–13] intense interest has been focus on applying V_2O_5 as a cathode material for rechargeable LIBs because of its high theoretical capacity, low cost, abundance, ease of synthesis, and better safety.[14–19] Unfortunately, until now, its practical application in rechargeable LIBs have been seriously hindered by its poor cycle stability, low electronic- and ionic conductivity, and sluggish electrochemical kinetics.[14] Therefore, it is highly desirable to simultaneously achieve the high-energy- and high-power density of V_2O_5 in cathode materials, but it remains a great challenge.

1D nanostructures, such as nanofibers, nanorods, and nanoribbons, have received increasing interest in energy-harvesting devices.[20] Furthermore, when electroactive materials possess porous and hollow 1D nanostructures, substantial improvements in power- and energy-density over bulk electrodes could be expected owing to the following advantages: 1) the 1D geometry could allow for efficient 1D electron transport along the longitudinal direction; 2) the hollow, porous structure would increase Li^+-ion flux at the interface between the active material and the electrode owing to the large surface-to-volume ratio with the electrolyte,[21–25] decrease the lithium-ion-diffusion length, and thus promote fast Li^+-ion transfer; 3) the 1D, porous nanostructure would also improve the structural stability against volume expansion, which would intrinsically improve the cycling stability. Although various methods to generate well-defined 1D nanostructures have been developed,[20–25] there are few re-

[a] Dr. H.-g. Wang, D.-l. Ma, Y. Huang, Prof. Dr. X.-b. Zhang
State Key Laboratory of Rare Earth Resource Utilization
Changchun Institute of Applied Chemistry
Chinese Academy of Sciences
Changchun, 130022 (P.R. China)
E-mail: xbzhang@ciac.jl.cn

[b] D.-l. Ma, Y. Huang
Key Laboratory of Automobile Materials
Ministry of Education and
School of Materials Science and Engineering
Jilin University, Changchun 130012 (P.R. China)

Supporting information for this article is available on the WWW under http://dx.doi.org/10.1002/chem.201200434.

ports of active materials that have porous and hollow 1D nanostructures,[26,27] to say nothing of controllable morphology as high-performance LIBs cathode materials that were prepared by a simple, versatile, and cost-effective technique.

As a remarkably simple and cost-effective technique, electrospinning has been used for many years to generate 1D inorganic/semiconductor nanomaterials with controllable morphology, various lengths, diameters, compositions, and complex architectures.[26–33] More importantly, besides the relatively high production rate and simplicity of the setup, the electrospun nanofibers possessed extremely high surface-to-volume ratios because of their superlong lengths and the porous substructure that was formed during the annealing process.[33] In view of these attractive features, many excellent efforts have been devoted to the design of high-performance metal-oxide-electrode materials by using the electrospinning technique. For example, Mai et al. have reported that ultralong hierarchical vanadium-oxide nanowires that were prepared by electrospinning could reduce the self-aggregation of the nanomaterials, thereby exhibiting improved performance for LIBs.[34] Recently, Srinivasan and co-workers prepared single-phase electrospun V_2O_5 nanofibers for LIBs.[35] However, these materials still suffered from serious disadvantages, such as low capacity and poor cycling stability, even at very low current densities. Therefore, it remains highly desirable and urgent to prepare high-performance electrode materials for LIBs with controlled morphology by using electrospinning techniques.

Herein, we used electrospinning techniques followed by controlled annealing in air to fabricate porous V_2O_5 nanotubes, hierarchical V_2O_5 nanofibers, and single-crystalline V_2O_5 nanobelts. To the best of our knowledge, this is the first synthesis of porous V_2O_5 nanotubes and single-crystalline V_2O_5 nanobelts by electrospinning. A detailed mechanism for the controlled formation of these morphologies by the general approach was also considered. In coin-cell measurements, these 1D V_2O_5 nanostructures exhibited high-performance as cathode materials for LIBs. Most importantly, the porous V_2O_5 nanotubes delivered a high power density (40.2 $kW\,kg^{-1}$), whilst the energy density remained high (up to 201 $Wh\,kg^{-1}$), which is one of the highest values on V_2O_5-based cathode materials. Interestingly, the beneficial crystal orientation of the single-crystalline V_2O_5 nanobelts provided improved cycling stability for lithium intercalation.

Results and Discussion

Scheme 1 shows the fabrication of porous V_2O_5 nanotubes, hierarchical V_2O_5 nanofibers, and single-crystalline V_2O_5 nanobelts based on a simple electrospinning method and subsequent annealing. These 1D V_2O_5 nanostructures were synthesized with high porosity, large surface areas, and short diffusion paths. Typically, the precursor nanofibers were electrospun from vanadium(IV)-acetylacetone/PVP/DMF at an appropriately high voltage. The obtained non-woven film was annealed at 400, 500, and 600 °C to afford porous V_2O_5 nanotubes, hierarchical V_2O_5 nanofibers, and single-crystalline V_2O_5 nanobelts, respectively.

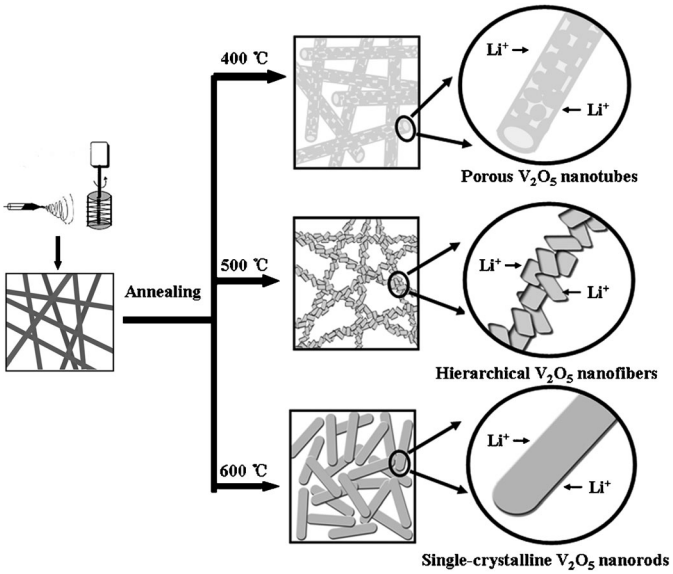

Scheme 1. Preparation of porous V_2O_5 nanotubes, hierarchical V_2O_5 nanofibers, and single-crystalline V_2O_5 nanobelts.

Figure 1 shows SEM images of the precursor nanofibers, porous V_2O_5 nanotubes, hierarchical V_2O_5 nanofibers, and single-crystalline V_2O_5 nanobelts. The precursor nanofibers had a relatively smooth surface with no pores or hierarchical nanostructure (Figure 1a). Close observation (Figure 1a, inset) revealed that the nanofibers had diameters of about 560 nm. After annealing, the continuous 1D nanostructures were retained, but there was a notable change to the surface and length of the nanofibers: There were many pores on the surface of the nanotubes with smaller diameters of about 340 nm (Figure 1b). On increasing the annealing temperature, the porous nanotubes were replaced by hierarchical nanofibers that were made up of attached V_2O_5 nanobelts

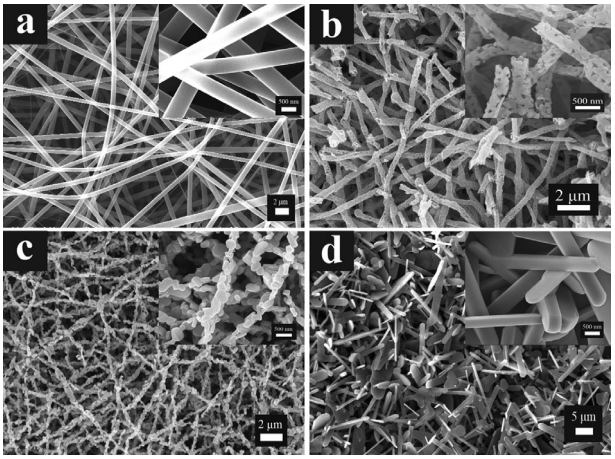

Figure 1. Low- and high-resolution SEM images (insets, scale bars: 500 nm) of: a) the precursor nanofibers and V_2O_5 nanostructures (scale bar: 2 μm) that were annealed at b) 400 °C (scale bar: 2 μm), c) 500 °C (scale bar: 2 μm), and d) 600 °C (scale bar: 5 μm).

(Figure 1c). Interestingly, a gradual increase in the annealing temperature resulted in the formation of nanobelts with a thickness of about 300 nm and a length of about 11 μm (Figure 1d). As a result, the morphology of the as-obtained V_2O_5 nanostructures could be controlled by adjusting the annealing treatment. The high porosity, large surface area, and hierarchical nanoarchitecture are very important for LIB materials.

Figure 2 shows the XRD patterns of the porous V_2O_5 nanotubes, hierarchical V_2O_5 nanofibers, and single-crystalline V_2O_5 nanobelts. All of the diffraction peaks were indexed to the pure orthogonal symmetry of V_2O_5 (space

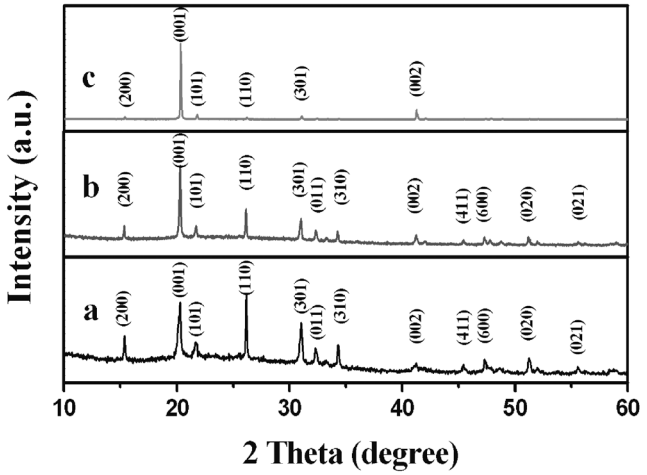

Figure 2. XRD patterns of V_2O_5 nanomaterials that were annealed at: a) 400 °C, b) 500 °C, and c) 600 °C.

group: *Pmmn* (no. 59); $a = 1.1516$, $b = 0.3565$, $c = 0.4372$ nm; JCPDS card no.: 41-1426). No other diffraction peaks were found, which indicated that the products were composed of pure V_2O_5. On increasing the annealing temperature, the intensities of the diffraction peaks increased, in particular the intensity of the (001) peak, thus indicating that the crystallization was enhanced and the crystallite-size increased. Thus, we concluded that the formation of single-crystalline V_2O_5 needed higher annealing temperatures.

To gain further insight into the morphology and structure of the V_2O_5 nanotube and nanobelt, TEM analysis was performed. The clear presence of nanotubes and nanobelts (Figure 3a–c) agreed with the SEM analysis. The high-resolution TEM (HRTEM) image of the nanobelt showed lattice fringes with a spacing of 0.58 nm, which was in good agreement with the spacing of the (200) planes of V_2O_5 (JCPDS card no. 41–1426; Figure 3d). The HRTEM image and fast Fourier transformation (FFT) pattern (Figure 3b, inset) confirmed that the resulting V_2O_5 nanobelt after annealing at 600 °C had a single-crystalline structure that was elongated along the [010] direction.

TGA was performed to investigate thermal decomposition as a function of the annealing temperature (Figure 4). The as-obtained precursor nanofibers underwent significant weight-loss owing to the decomposition of vanadium(IV)

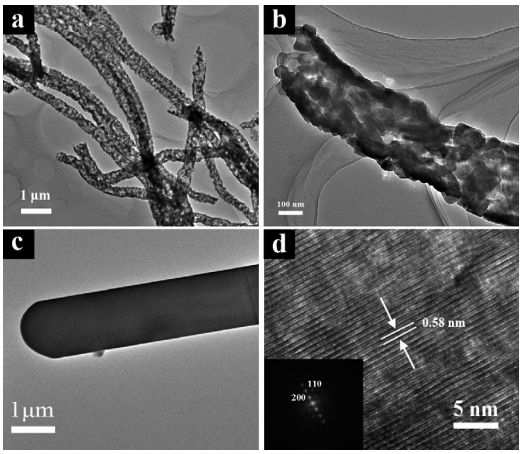

Figure 3. a) Low-, and b) high-resolution TEM images of porous V_2O_5 nanotubes (scale bar: 100 nm); c) TEM image of a single V_2O_5 nanobelt; d) HRTEM image of the nanobelt lattice. Inset: the corresponding fast Fourier-transfer transformation pattern.

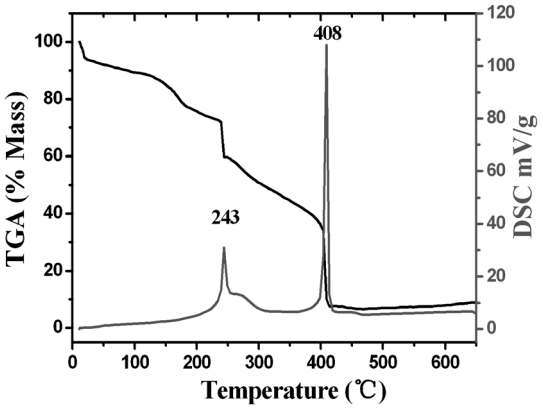

Figure 4. Thermogravimetric analysis (TGA) of the as-prepared vanadium(IV)-acetylacetone/PVP precursor nanofibers.

acetylacetone and PVP during the heat treatment, thereby leading to significant volume shrinkage and the formation of V_2O_5 nanostructures. There was a mass-loss below 200 °C that was attributed to the loss of adsorbed water and residual solvent (DMF). At 243 °C, there was a dramatic mass-loss that was accompanied by an exothermic DSC peak. These features corresponded to the decomposition of vanadium(IV) acetylacetone and the degradation of PVP, which had two degradation mechanisms that involved both intra- and intermolecular-transfer reactions.[36] The following mass-loss, which was accompanied by an exothermic peak at 408 °C, was due to the oxidation of carbon and carbon monoxide that was released by the decomposition of polymeric residues.[37]

To gain further insight into the evolution of the V_2O_5 nanostructures, a series of temperature-dependent experiments were conducted and the intermediate solids at different annealing temperature were examined. Based on the temperature-dependent experiments, we proposed a possible mechanism to explain the formation of these V_2O_5 nanostructures; Figure 5 shows representative SEM images for

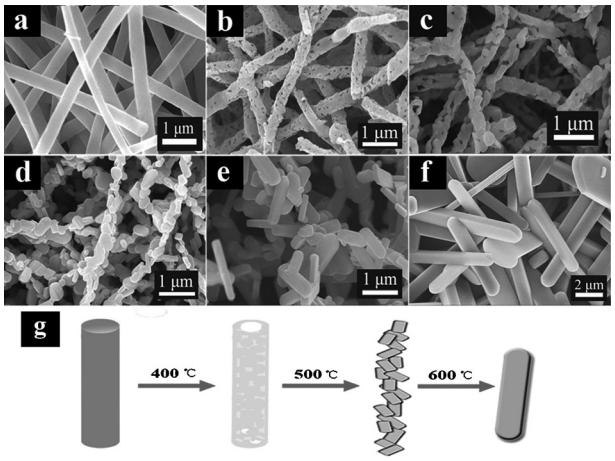

Figure 5. SEM images of V_2O_5 nanostructures that were annealed at: a) 350 °C, b) 400 °C, c) 450 °C, d) 500 °C, e) 550 °C, and f) 600 °C; g) formation of V_2O_5 nanostructures.

samples that were collected after stepwise annealing at 350, 400, 450, 500, 550, and 600 °C. These sequential images revealed a morphological evolution from nanofibers into porous nanotubes, then hierarchical nanofibers, and finally into nanobelts. After annealing at 350 °C, the obtained V_2O_5 nanofibers had an average diameter of about 410 nm and a relatively smooth surface without any pores or hierarchical nanostructures (Figure 5a). After slowly annealing to 400 °C, at which point significant weight-loss was observed in the TGA profile, porous V_2O_5 nanotubes were obtained (Figure 5b). Again, these nanotubes were long and continuous and the diameter had shrunk to about 50 nm, owing to the decomposition of the PVP polymer template. Upon sintering in air, the degradation of PVP and the growth of the V_2O_5 nanoparticles occurred simultaneously. On increasing the temperature, PVP would be oxidized into CO_2 and rapidly volatilized, whilst vanadium(IV) acetylacetone was oxidized into V_2O_5 nanoparticles on the surface of the fibers. The outward diffusion of CO_2 generated a force to compress the V_2O_5 nanoparticles in the surface region into a shell. The porous shell allowed CO_2 effusion from the regions below the shell. The vanadium(IV) precursor in the inner part of the fibers would move towards the surface, presumably accelerated by gaseous species that were produced by the oxidation of PVP, and crystallize into V_2O_5. Finally, these nanoparticles would become connected together to generate porous V_2O_5 nanotubes.[26,33] When the annealing temperature was raised to 450 °C, the porous V_2O_5 nanotubes were retained; however, the growth of individual V_2O_5 nanograins was required by consuming nearby materials, which simultaneously triggered the formation of nanograin spacing (Figure 5c), thereby indicating that the continuous grain growth at higher annealing temperature would eventually create spacings between the nanograins. However, by further increasing the annealing temperature to 500 °C, the continuous grain growth resulted in the disappearance of the spacings between the nanograins.[31,33] As a result, the porous nanotubes were replaced by hierarchical nanofibers that were made up of attached V_2O_5 nanobelts (Figure 5d). Above 500 °C, the increase in annealing temperature progressively encouraged the growth of V_2O_5 nanobelts; as a result, the fiber scaffold was virtually destroyed (Figure 5e, f). During extended annealing, the transformation of smaller nanobelts into larger ones occurred. The quantity of nanobelts per unit of area became fewer, which indicated that some small nanobelts were consumed to promote the further growth of larger ones (Figure 4e, f).

Based on the above analysis, the evolution of V_2O_5 nanostructures was divided into three processes as follows (Figure 5g): At annealing temperatures below 400 °C, the temperature was not high enough to promote the complete decomposition of the PVP polymer template. At this point, the obtained nanofibers still possessed a relatively smooth surface without any pores or hierarchical nanostructures. Between 400 and 450 °C, the complete degradation of PVP and the growth of V_2O_5 nanograins created internal pores and spacings between the nanograins, thereby resulting in the formation of porous V_2O_5 nanotubes. Above 450 °C, continuous grain growth resulted in the disappearance of the porous nanotubes and even the fiber scaffold became damaged, thereby realizing the transformation from nanotubes into nanobelts. Clearly, the annealing temperature was crucial to controlling the morphology of the V_2O_5 nanostructures.

Next, we investigate the electrochemical performance of these V_2O_5 nanostructures as cathode materials for LIBs. Figure 6a shows cyclic voltammetry (CV) curve of the porous V_2O_5 nanotubes. Two pairs of redox peaks (at about 3.4 V and 3.2 V) were observed that are commonly ascribed to phase transitions from α-V_2O_5 into ε-$Li_{0.5}V_2O_5$ and δ-LiV_2O_5, as shown in Equations (1) and (2), respectively.[16,38]

$$V_2O_5 + 0.5\,Li^+ + 0.5e^- \rightleftharpoons \varepsilon\text{-}Li_{0.5}V_2O_5 \quad (1)$$

$$\varepsilon\text{-}Li_{0.5}V_2O_5 + 0.5\,Li^+ + 0.5\,e^- \rightleftharpoons \delta\text{-}LiV_2O_5 \quad (2)$$

Figure 6b shows the initial charge/discharge curves of the porous V_2O_5 nanotubes at various current densities in the range 2.5–4.0 V. Both the charge and discharge curves showed two voltage plateaus, which was consistent with the CV analysis (see above). The initial discharge and charge capacities were 139.8 and 145 mAh g^{-1} at 0.1 A g^{-1}, respectively, which was close to its theoretical capacity (148 mAh g^{-1}) with 1 Li-insertion/extraction per unit formula. When the discharge-current density was increased to 2 A g^{-1}, the V_2O_5 nanotubes gave a capacity of about 131.2 mAh g^{-1}. By further increasing the current density to 6 A g^{-1}, a capacity of 114.1 mAh g^{-1} was still delivered. Apart from the high reversible capacity, the V_2O_5 nanotubes showed superior cycling performance. As shown in Figure 6c, the capacity remained at about 80.5 % (75.4 %) after 250 cycles at a high current density of 2 A g^{-1} (4 A g^{-1}). Most importantly, even at high current densities (6 A g^{-1}), the V_2O_5 nanotubes still exhibited good cyclic-capacity retention (71.9 %) after

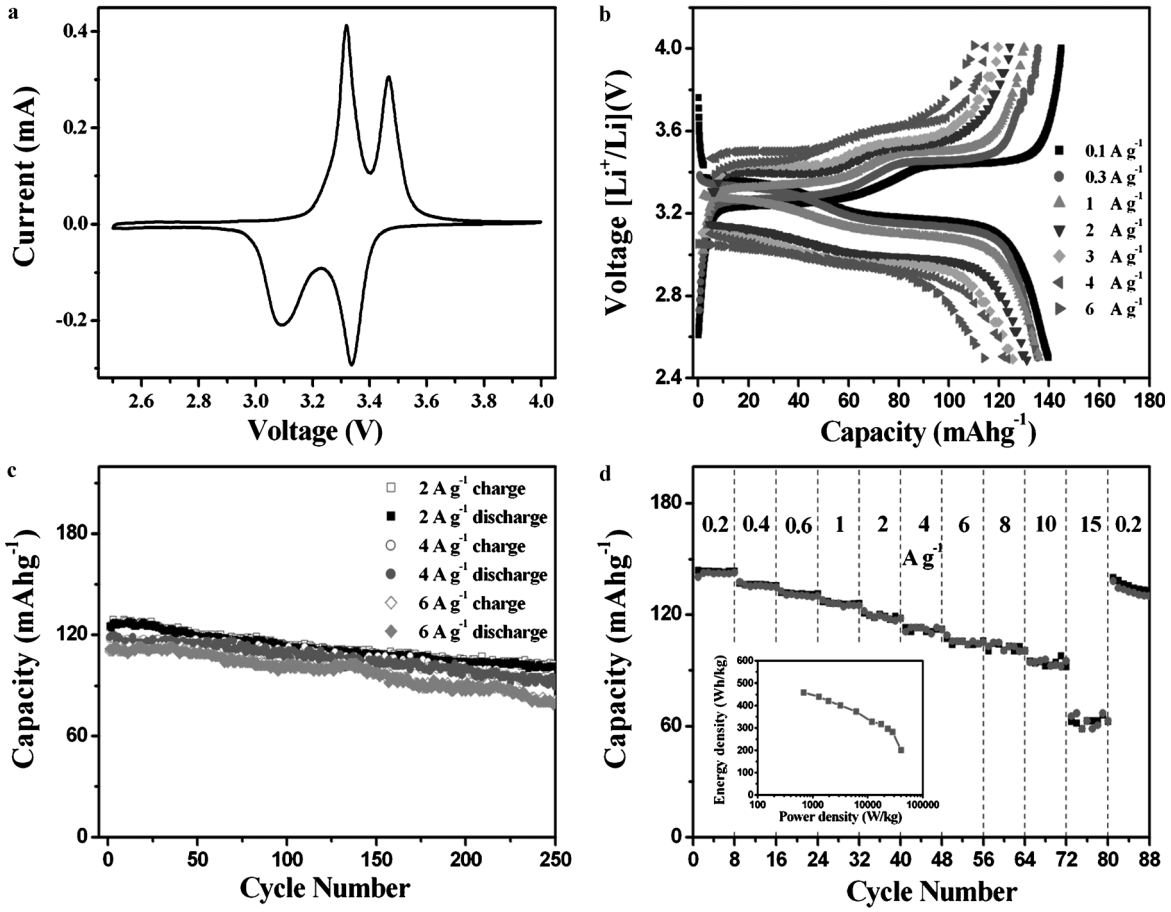

Figure 6. a) Cyclic voltammetry (CV) of the porous V_2O_5 nanotubes at a scan rate of 0.1 mV s^{-1}; b) initial galvanostatic charge/discharge curves; c) cycling performance; and d) rate performance of the porous V_2O_5 nanotubes at different current densities in the range 2.5–4.0 V; inset: Ragone plots.

250 cycles. When the voltage range was extended to 2.0–4.0 V, the capacity increased to 276.2 mAh g^{-1} at a current density of 1 A g^{-1}, which meant that the V_2O_5 nanotubes could be discharged to a lithiated state of γ-$Li_2V_2O_5$ (see the Supporting Information, Figure S1a). Although the V_2O_5 nanotubes had a large capacity (theoretical capacity of 297 mAh g^{-1} in the voltage range 2.0–4.0 V), the cycling stability was not satisfactory because the capacity decreased very fast (see the Supporting Information, Figure S1b). In addition, the charge/discharge profiles between 2.5 and 4.0 V showed narrow gaps, thereby indicating a low electrode resistance, which was helpful for achieving high power density.[39] Figure 6d shows the outstanding high-power- and high-energy performance of the V_2O_5 nanotubes electrode. At a current density of 15 A g^{-1}, the V_2O_5-nanotubes electrode delivered a discharge capacity of 65.2 mAh g^{-1}, which corresponded to a discharge energy density of 201 W h kg^{-1} and a power density of about 40.2 kW kg^{-1}; this value is one of the highest power densities on V_2O_5-based cathode materials. The excellent electrochemical performance was ascribed to the unique porous-nanotube structure that provided efficient 1D electron transport along the longitudinal direction, short distances for Li^+-ion diffusion, and large electrode–electrolyte contact area for high Li^+-ion flux across the interface, which allowed the material to effectively buffer the stress that was induced during the charge/discharge process.

We also investigated the lithium-storage properties of our hierarchical V_2O_5 nanofibers. Figure 7a shows the charge/discharge curves of the hierarchical V_2O_5 nanofibers at various current densities in the range 2.5–4.0 V. The initial discharge and charge capacities were 116.3 and 117.6 mAh g^{-1} at 0.2 A g^{-1}, 91.4 and 92 mAh g^{-1} at 2 A g^{-1}, and 80.3 and 82 mAh g^{-1} at 6 A g^{-1}, respectively. Figure 7b shows the cycling performance of the hierarchical V_2O_5 nanofibers. Also, the hierarchical V_2O_5 nanofibers showed stable capacities of about 78.1 mAh g^{-1} (85.4% of initial discharge capacity) and 73.4 mAh g^{-1} (81.6% of initial discharge capacity) over up to 250 cycles at 2 and 3 A g^{-1}, respectively. When compared to the porous V_2O_5 nanotubes, the hierarchical V_2O_5 nanofibers exhibited a slightly lower capacity but better cyclic performance (see the Supporting Information, Figure S2). These results may have been due to the shape transformation, as well as the beneficial crystal orientation that resulted from the high annealing temperature. To confirm this hypothesis, it was necessary to investigate the cycling performance of the single-crystalline V_2O_5 nanobelts that were annealed at 600 °C.

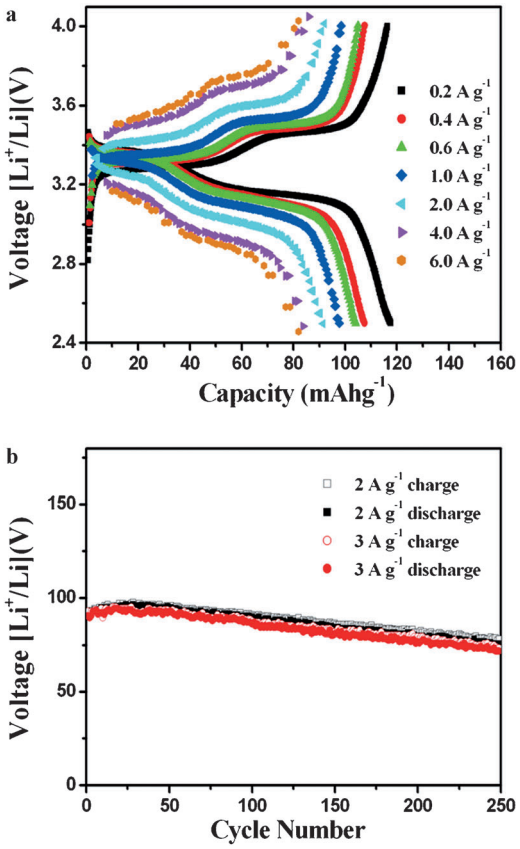

Figure 7. a) Initial galvanostatic charge/discharge curves, and b) cycling performance of hierarchical V_2O_5 nanofibers at different current densities in the range 2.5–4.0 V.

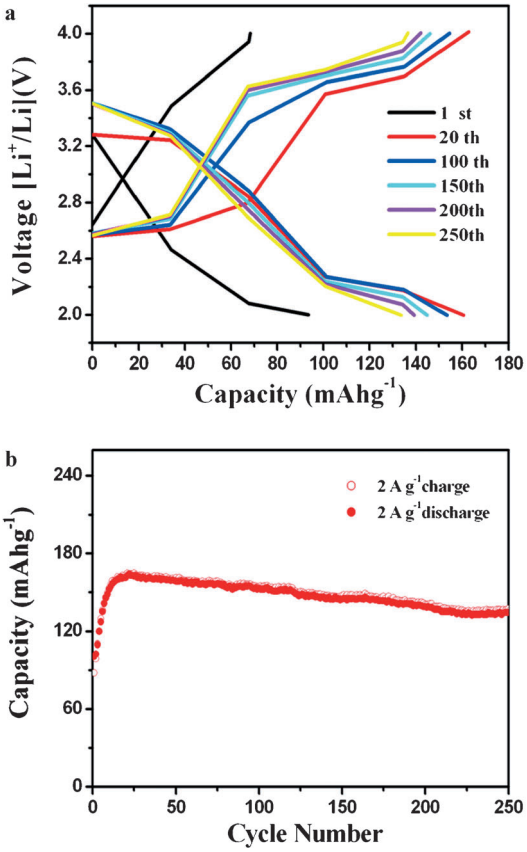

Figure 8. a) Galvanostatic charge/discharge curves, and b) cycling performance of single-crystalline V_2O_5 nanobelts in the range 2.0–4.0 V (current density: 2 A g^{-1}).

Comparison of the cycling performance of the different nanostructures showed that the single-crystalline V_2O_5 nanobelts exhibited superior cyclic-capacity retention over the porous V_2O_5 nanotubes and hierarchical V_2O_5 nanofibers (see the Supporting Information, Figure S3). Figure 8a shows the discharge/charge curves of the single-crystalline V_2O_5 nanobelts at a current density of 2 A g^{-1} in the range 2.0–4.0 V. Interestingly, the electrode exhibited increasing capacity with cycling over the first 20 cycles, which may have been due to some long-term activation during charge/discharge cycling.[40,41] After the first 20 cycles, the specific capacity of the single-crystalline V_2O_5 nanobelts (162.8 mAh g^{-1}) began to decline and was 137.8 mAh g^{-1} after 250 cycles, which corresponded to a loss of 15% (Figure 8b). This superior cycling performance could be attributed to the beneficial crystal orientations, with suppressed thickness along the [001] direction, which could withstand significant stress without disintegration.[42] After the 100th cycle, the single-crystalline V_2O_5 nanobelts still maintained a thin belt-like structure (see the Supporting Information, Figure S4). These results suggested that the single-crystalline nanobelts could efficiently inhibit the volume-change and aggregation of the V_2O_5 electrode materials, thus retaining their stability to some extent during the lithiation and delithiation processes. These results confirmed that the single-crystalline V_2O_5 nanobelts along the [001] direction possessed greatly enhanced electrochemical properties. The only "fly in the ointment" was the lower specific capacity (Figure 8; also see the Supporting Information, Figure S5). Our current work is focused on improving the specific capacity of the single-crystalline V_2O_5 nanobelts.

Conclusion

We have demonstrated a facile and effective "electrospinning technique and subsequent annealing treatment" strategy for the controllable synthesis of porous V_2O_5 nanotubes, hierarchical V_2O_5 nanofibers, and single-crystalline V_2O_5 nanobelts. The uniqueness of this strategy was that the morphology of the nanostructures could be tailored by adjusting the annealing temperature. As potential cathode materials for LIBs, the as-formed V_2O_5 nanostructures exhibited highly reversible capacities and superior cycling performance. This excellent electrochemical performance was ascribed to their unique 1D nanostructure, which improved electrolyte infiltration and facilitated Li-ion diffusion in the electrode. These results demonstrated that further improvement or optimization of the electrochemical performance of transition-metal-oxide-based electrode materials could be

realized by the design of 1D nanostructures with unique morphology. This facile strategy could be extended to the synthesis of other materials with controlled morphology, as well as applications in electrochemical capacitors, sensors, and catalysts.

4. Experimental Section

Materials and synthesis: Vanadium(IV) acetylacetone was synthesized according to a literature procedure.[43] In a typical synthesis, polyvinylpyrrolidone (PVP, $M_w = 1\,300\,000$, 0.5 g) and vanadium(IV) acetylacetone (0.3978 g) were dissolved in DMF (2.5 g) under vigorous stirring. Next, the viscous hybrid solution was loaded into a plastic syringe that was equipped with a 9-gauge stainless steel nozzle. The solution was electrospun at a DC voltage of 15 kV and a flow rate of 1.0 mL h^{-1}. The electrospun nanofibers were collected on aluminum foil that was placed 15 cm between the nozzle and collector. Finally, the as-collected films were annealed in a tube furnace at different temperatures (1 °C min^{-1}).

Characterization: The morphology and crystalline structure of the as-obtained samples were characterized by SEM (Hitachi S-4800) and TEM on a Tecnai G2 that was operating at 200 kV. X-ray diffraction (XRD) patterns were recorded on a Rigaku-Dmax 2500 diffractometer with Cu Kα radiation. TGA and differential thermal analysis (DTA) were carried out on a TA SDT 2960 simultaneous thermal analyzer in air with a heating rate of 10 °C min^{-1}.

Electrochemistry: The electrodes were prepared by mixing the active materials (70 wt.%), acetylene black (20 wt.%), and polyvinylidene fluoride (PVDF, 10 wt.%) in *N*-methyl-2-pyrrolidone (NMP). After the slurries had been uniformly spread over aluminum foil, the electrodes were dried at 80 °C in a vacuum for 6 h. Next, the electrodes were pressed and cut into disks before transferring into an argon-filled glove box. Coin cells (CR2025) were laboratory-assembled by using lithium metal as the counter electrode, Celgard 2400 membrane as the separator, and $LiPF_6$ (1 M in ethylene-carbonate/dimethyl-carbonate, EC/DMC, 1:1 v/v) as the electrolyte. Galvanostatic charge/discharge tests were carried out on a Land Battery Measurement System (Land, China). CV and impedance tests were performed on a VMP3 Electrochemical Workstation (Bio-logic Inc.).

Acknowledgements

This work was supported by the 100 Talents Program of the Chinese Academy of Sciences, the National Natural Science Foundation of China (grant no. 21101147), the Jilin Province Science and Technology Development Program (grant no. 20100102 and 20116008), and by the Heilongjiang Province Science and Technology project (grant no. GC09A403).

[1] J. B. Goodenough, Y. Kim, *Chem. Mater.* **2010**, *22*, 587.
[2] M. S. Whittingham, *Chem. Rev.* **2004**, *104*, 4271.
[3] M. Morcrette, P. Rozier, L. Dupont, E. Mugnier, L. Sannier, J. Galy, J. M. Tarascon, *Nat. Mater.* **2003**, *2*, 755.
[4] Y. Oumellal, A. Rougier, G. A. Nazri, J. M. Tarascon, L. Aymard, *Nat. Mater.* **2008**, *7*, 916.
[5] S. Y. Chung, J. T. Bloking, Y. M. Chiang, *Nat. Mater.* **2002**, *1*, 123.
[6] X. P. Gao, H. X. Yang, *Energy Environ. Sci.* **2010**, *3*, 174.
[7] B. L. Ellis, K. T. Lee, L. F. Nazar, *Chem. Mater.* **2010**, *22*, 691.
[8] G. Gu, M. Schmid, P. W. Chiu, A. Minett, J. Fraysse, G. T. Kim, S. Roth, M. Kozlov, E. Munoz, R. H. Baughman, *Nat. Mater.* **2003**, *2*, 316.
[9] M. Ponzi, C. Duschatzky, A. Carrascull, E. Ponzi, *Appl. Catal. A* **1998**, *169*, 373.
[10] J. Liu, X. Wang, Q. Peng, Y. Li, *Adv. Mater.* **2005**, *17*, 764.
[11] M. S. Whittingham, *J. Electrochem. Soc.* **1976**, *123*, 315.
[12] D. M. Yu, C. G. Chen, S. H. Xie, Y. Y. Liu, K. Park, X. Y. Zhou, Q. F. Zhang, J. Y. Li, G. Z. Cao, *Energy Environ. Sci.* **2011**, *4*, 858.
[13] N. A. Chernova, M. Roppolo, A. C. Dillon, M. S. Whittingham, *J. Mater. Chem.* **2009**, *19*, 2526.
[14] D. W. Liu, G. Z. Cao, *Energy Environ. Sci.* **2010**, *3*, 1218.
[15] Y. Wang, K. Takahashi, K. Lee, G. Z. Cao, *Adv. Funct. Mater.* **2006**, *16*, 1133.
[16] A. M. Cao, J. S. Hu, H. P. Liang, L. J. Wan, *Angew. Chem.* **2005**, *117*, 4465; *Angew. Chem. Int. Ed.* **2005**, *44*, 4391.
[17] Y. S. Hu, X. Liu, J. O. Müller, R. Schlögl, J. Maier, D. S. Su, *Angew. Chem.* **2008**, *121*, 216; *Angew. Chem. Int. Ed.* **2008**, *48*, 210.
[18] P. X. Han, Y. H. Yue, Z. H. Liu, W. Xu, L. X. Zhang, H. X. Xu, S. M. Dong, G. L. Cui, *Energy Environ. Sci.* **2011**, *4*, 4710.
[19] Y. Wang, H. J. Zhang, W. X. Lim, J. Y. Lin, C. C. Wong, *J. Mater. Chem.* **2011**, *21*, 2362.
[20] G. Z. Cao, *Nanostructures and Nanomaterials, Synthesis, Properties and Applications*, Imperial College, London, **2004**.
[21] W. M. Zhang, X. L. Wu, J. S. Hu, Y. G. Guo, L. J. Wan, *Adv. Funct. Mater.* **2008**, *18*, 3941.
[22] C. K. Chan, H. L. Peng, G. Liu, K. McIlwrath, X. F. Zhang, R. A. Huggins, Y. Cui, *Nat. Nanotechnol.* **2007**, *2*, 31.
[23] S. Dong, X. Chen, L. Gu, X. Zhou, L. Li, Z. Liu, P. Han, H. Xu, J. Yao, H. Wang, X. Zhang, C. Shang, G. Cui, L. Chen, *Energy Environ. Sci.* **2011**, *4*, 3502.
[24] S. Ding, J. S. Chen, X. W. Lou, *Adv. Funct. Mater.* **2011**, *21*, 4120.
[25] Z. Wang, D. Luan, S. Madhavi, C. M. Li, X. W. Lou, *Chem. Commun.* **2011**, *47*, 8061.
[26] L. M. Li, X. M. Yin, S. Liu, Y. G. Wang, L. B. Chen, T. H. Wang, *Electrochem. Commun.* **2010**, *12*, 1383.
[27] M. Shang, W. Z. Wang, W. Z. Yin, J. Ren, S. M. Sun, L. Zhang, *Chem. Eur. J.* **2010**, *16*, 11412.
[28] L. W. Ji, Z. Lin, A. J. Medford, X. W. Zhang, *Chem. Eur. J.* **2009**, *15*, 10718.
[29] D. Li, Y. Xia, *Nano Lett.* **2003**, *3*, 555.
[30] L. W. Ji, Z. Lin, B. K. Guo, A. J. Medford, X. W. Zhang, *Chem. Eur. J.* **2010**, *16*, 11543.
[31] L. Xu, H. W. Song, B. Dong, Y. Wang, J. Chen, X. Bai, *Inorg. Chem.* **2010**, *49*, 10590.
[32] W. Luo, X. L. Hu, Y. M. Sun, Y. H. Huang, *Phys. Chem. Chem. Phys.* **2011**, *13*, 16735.
[33] W. S. Chen, D. A. Huang, H. C. Chen, T. Y. Shie, C. H. Hsieh, J. D. Liao, C. Kuo, *Cryst. Growth Des.* **2009**, *9*, 4070.
[34] L. Mai, L. Xu, C. Han, X. Xu, Y. Luo, S. Zhao, Y. Zhao, *Nano Lett.* **2010**, *10*, 4750.
[35] Y. L. Cheah, N. Gupta, S. S. Pramana, V. Aravindan, G. Wee, M. Srinivasan, *J. Power Sources* **2011**, *196*, 6465.
[36] S. J. Azhari, M. A. Diab, *Polym. Degrad. Stab.* **1998**, *60*, 253.
[37] Z. L. Wang, X. J. Liu, M. F. Lv, P. Chai, Y. Liu, J. Meng, *J. Phys. Chem. B* **2008**, *112*, 11292.
[38] X. F. Zhang, K. X. Wang, X. Wei, J. S. Chen, *Chem. Mater.* **2011**, *23*, 5290.
[39] J. Yan, A. Sumboja, E. Khoo, P. S. Lee, *Adv. Mater.* **2011**, *23*, 746.
[40] J. S. Chen, Y. L. Cheah, S. Madhavi, X. W. Lou, *J. Phys. Chem. C* **2010**, *114*, 8675.
[41] L. Q. Mai, B. Hu, W. Chen, Y. Y. Qi, C. S. Lao, R. S. Yang, Y. Dai, Z. L. Wang, *Adv. Mater.* **2007**, *19*, 3712.
[42] A. M. Glushenkov, V. I. Stukachev, M. F. Hassan, G. G. Kuvshinov, H. K. Liu, Y. Chen, *Cryst. Growth Des.* **2008**, *8*, 3661.
[43] J. Liu, H. Xia, D. F. Xue, L. Lu, *J. Am. Chem. Soc.* **2009**, *131*, 12086.

Received: February 10, 2012
Revised: April 6, 2012
Published online: ■■ ■■, 0000

Nanostructures

*H.-g. Wang, D.-l. Ma, Y. Huang, X.-b. Zhang** ..... ▮▮▮▮–▮▮▮▮

Electrospun V_2O_5 Nanostructures with Controllable Morphology as High-Performance Cathode Materials for Lithium-Ion Batteries

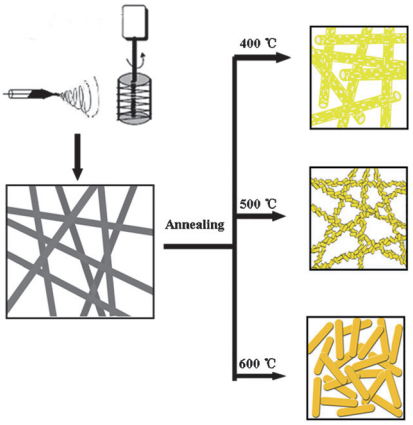

Assault and batteries: Porous V_2O_5 nanotubes, hierarchical V_2O_5 nanofibers, and single-crystalline V_2O_5 nanobelts were controllably synthesized. When tested as the cathode materials in lithium-ion batteries, the as-formed V_2O_5 nanostructures exhibited highly reversible capacity, excellent cycling performance, and good rate capacity.

